Dark matter, Z', and vector-like quark at the LHC and $b \to s\mu\mu$ anomaly*

Wei Chao(晁伟)[1] Hong-Xin Wang(王宏昕)[2] Lei Wang(王磊)[2†] Yang Zhang(张阳)[3]

[1]Center for Advanced Quantum Studies, Department of Physics, Beijing Normal University, Beijing 100875, China
[2]Department of Physics, Yantai University, Yantai 264005, China
[3]School of Physics and Microelectronics, Zhengzhou University, ZhengZhou 450001, China

Abstract: Combining the $b \to s\mu^+\mu^-$ anomaly and dark matter observables, we study the capability of the LHC to test dark matter, Z', and a vector-like quark. We focus on a local $U(1)_{L_\mu - L_\tau}$ model with a vector-like $SU(2)_L$ doublet quark Q and a complex singlet scalar whose lightest component X_I is a candidate of dark matter. After imposing relevant constraints, we find that the $b \to s\mu^+\mu^-$ anomaly and the relic abundance of dark matter favor $m_{X_I} < 350$ GeV and $m_{Z'} < 450$ GeV for $m_Q < 2$ TeV and $m_{X_R} < 2$ TeV (the heavy partner of m_{X_I}). Current searches for jets and missing transverse momentum at the LHC sizably reduce the mass ranges of the vector-like quark, and m_Q is required to be larger than 1.7 TeV. Finally, we discuss the possibility of probing these new particles at the high luminosity LHC via the QCD process $pp \to D\bar{D}$ followed by $D \to s(b)X_I$, $D \to s(b)Z'X_I$, and then $Z' \to \mu^+\mu^-$. Taking a benchmark point of m_Q = 1.93 TeV, $m_{Z'}$ = 170 GeV, and m_{X_I} = 145 GeV, we perform a detailed Monte Carlo simulation and find that this benchmark point can be accessed at the 14 TeV LHC with an integrated luminosity of 3000 fb^{-1}.

Keywords: new physics model, dark matter, b meson anomaly

DOI: 10.1088/1674-1137/ac06ba

I. INTRODUCTION

At present, there are several interesting excesses in B-physics measurements involving the transition $b \to s\ell^+\ell^-$ $(\ell = \mu, e)$

$$R_{K^{(*)}} \equiv \frac{B \to K^{(*)}\mu^+\mu^-}{B \to K^{(*)}e^+e^-}. \tag{1}$$

The LHCb results for the R_K ratio in one q_2 bin [1, 2] and the R_{K^*} ratio in two q_2 bins [3] were found to lie significantly below one:

$$\begin{aligned} &R_K = 0.846^{+0.060}_{-0.054}(\text{stat})^{+0.016}_{-0.014}(\text{syst}),\\ &q^2 \in [1,6]\ \text{GeV}^2,\\ &R_{K^*} = 0.660^{+0.110}_{-0.070}(\text{stat}) \pm 0.024(\text{syst}),\\ &q^2 \in [0.045, 1.1]\ \text{GeV}^2,\\ &R_{K^*} = 0.685^{+0.113}_{-0.069}(\text{stat}) \pm 0.047(\text{syst}),\\ &q^2 \in [1.1, 6.0]\ \text{GeV}^2. \end{aligned} \tag{2}$$

Belle announced its measurement of R_{K^*} [4]:

$$R_{K^*} = \begin{cases} 0.52^{+0.36}_{-0.26} \pm 0.05\,, & 0.045 \leqslant q^2 \leqslant 1.1\ \text{GeV}^2\,,\\ 0.96^{+0.45}_{-0.29} \pm 0.11\,, & 1.1 \leqslant q^2 \leqslant 6.0\ \text{GeV}^2\,,\\ 0.90^{+0.27}_{-0.21} \pm 0.10\,, & 0.1 \leqslant q^2 \leqslant 8.0\ \text{GeV}^2\,,\\ 1.18^{+0.52}_{-0.32} \pm 0.10\,, & 15.0 \leqslant q^2 \leqslant 19.0\ \text{GeV}^2\,,\\ 0.94^{+0.17}_{-0.14} \pm 0.08\,, & 0.045 \leqslant q^2\,. \end{cases} \tag{3}$$

Global fits to the experimental data show that a new physics model can explain the anomalies of $R(K)$ and $R(K^*)$ by contributing to C_9^μ. With $C_{10}^{\mu,\text{NP}} = 0$, the best fit value for $C_9^{\mu,\text{NP}}$ is -1.10 ± 0.16 [5].

A $U(1)_{L_\mu - L_\tau}$ gauge boson couples only to $\mu(\tau)$ but not to an electron [6], and this type of $U(1)_{L_\mu - L_\tau}$ model has also been modified from its minimal version to explain the $b \to s\mu^+\mu^-$ anomaly [7-23]. In Ref. [23], in addition to the $U(1)_{L_\mu - L_\tau}$ gauge boson Z' and a complex singlet S breaking $U(1)_{L_\mu - L_\tau}$ symmetry, a vector-like $SU(2)_L$ doublet quark Q and a complex singlet X are introduced

Received 21 February 2021; Accepted 1 June 2021; Published online 2 July 2021
* Supported by the National Natural Science Foundation of China (11975013, 11775025), the Natural Science Foundation of Shandong province (ZR2017JL002, ZR2017MA004) and the Project of Shandong Province Higher Educational Science and Technology Program (2019KJJ007)
† E-mail: leiwang@ytu.edu.cn

to produce a $Z'bs$ coupling large enough to explain the anomalies of $R(K^{(*)})$. As the lightest component of X, X_I is a candidate of dark matter (DM). In this study, we combine the $b\to s\mu^+\mu^-$ anomaly and DM experimental data to study the capability of the LHC to test dark matter, Z', and vector-like quarks.

Our work is organized as follows. In Sec. II, we recapitulate the model. In Sec. III, we consider relevant theoretical constraints and $b\to s$ flavor observables and explain the $b\to s\mu^+\mu^-$ anomaly. In Sec. IV, we discuss DM observables. In Sec. V, we use the current searches at the LHC to constrain the parameter space and analyze the possibility of probing the new particles at the high luminosity LHC. Finally, we give our conclusion in Sec. VI.

II. THE MODEL

In addition to the $U(1)_{L_\mu-L_\tau}$ gauge boson Z', the model predicts a complex singlet $\mathcal{S}$, a complex singlet X, and an $SU(2)_L$ doublet quark Q. Their quantum numbers under the gauge group $SU(3)_C\times SU(2)_L\times U(1)_Y\times U(1)_{L_\mu-L_\tau}$ are shown in Table 1.

The Lagrangian which remains invariant under the $SU(3)_C\times SU(2)_L\times U(1)_Y\times U(1)_{L_\mu-L_\tau}$ symmetry is given by

$$\begin{aligned}\mathcal{L}=&\mathcal{L}_{\rm SM}-\frac{1}{4}Z'_{\mu\nu}Z'^{\mu\nu}+g_{Z'}Z'^{\mu}(\bar\mu\gamma_\mu\mu+\bar\nu_{\mu_L}\gamma_\mu\nu_{\mu_L}-\bar\tau\gamma_\mu\tau\\&-\bar\nu_{\tau_L}\gamma_\mu\nu_{\tau_L})-V+\bar Q(i\not{D}-M_Q)Q+(D_\mu X^\dagger)(D^\mu X)\\&+(D_\mu\mathcal{S}^\dagger)(D^\mu\mathcal{S})-\sum_{i=1}^{3}(\lambda_i\bar q_L^iQX+{\rm h.c.}).\end{aligned}\tag{4}$$

Here, we ignore the kinetic mixing term of gauge bosons of $U(1)_{L_\mu-L_\tau}$ and $U(1)_Y$. q_L^i denotes the SM left-handed quark doublet with $i=1,2,3$, and D_μ is the covariant derivative. The field strength tensor is $Z'_{\mu\nu}=\partial_\mu Z'_\nu-\partial_\nu Z'_\mu$, and $g_{Z'}$ is the gauge coupling constant of the $U(1)_{L_\mu-L_\tau}$ group. The scalar potential V is given by

$$\begin{aligned}V=&-\mu_h^2(H^\dagger H)-\mu_S^2(\mathcal{S}^\dagger\mathcal{S})+m_X^2(X^\dagger X)+\left[\mu X^2\mathcal{S}+{\rm h.c.}\right]\\&+\lambda_H(H^\dagger H)^2+\lambda_S(\mathcal{S}^\dagger\mathcal{S})^2+\lambda_X(X^\dagger X)^2+\lambda_{SX}(\mathcal{S}^\dagger\mathcal{S})(X^\dagger X)\\&+\lambda_{HS}(H^\dagger H)(\mathcal{S}^\dagger\mathcal{S})+\lambda_{HX}(H^\dagger H)(X^\dagger X).\end{aligned}\tag{5}$$

Table 1. Quantum numbers of the vector-like quark $Q\equiv(U,D)$ and scalars X and S under the gauge group $SU(3)_C\times SU(2)_L\times U(1)_Y\times U(1)_{L_\mu-L_\tau}$.

	$SU(3)_c$	$SU(2)_L$	$U(1)_Y$	$U(1)_{L_\mu-L_\tau}$
Q	**3**	**2**	+1/6	$-q_x$
X	**1**	**1**	0	q_x
$\mathcal{S}$	**1**	**1**	0	$-2q_x$

The SM Higgs doublet H, the singlet filed $\mathcal{S}$, and X are expressed as

$$H=\begin{pmatrix}G^+\\ \frac{1}{\sqrt2}(h_1+v_h+{\rm i}G)\end{pmatrix},\mathcal{S}=\frac{1}{\sqrt2}(h_2+v_S+{\rm i}\omega),\quad X=\frac{1}{\sqrt2}(X_R+{\rm i}X_I),\tag{6}$$

where $v_h=246$ GeV and v_S are, respectively, vacuum expectation values (VEVs) of H and $\mathcal{S}$, and the X field has no VEV. The mass parameters μ_h^2 and μ_S^2 in the potential of Eq. (5) are determined by the potential minimization conditions:

$$\begin{aligned}\mu_h^2&=\lambda_H v_h^2+\frac12\lambda_{HS}v_S^2,\\ \mu_S^2&=\lambda_S v_S^2+\frac12\lambda_{HS}v_h^2.\end{aligned}\tag{7}$$

After $\mathcal{S}$ acquires the VEV, the μ term splits the complex scalar X into two real scalar fields X_R and X_I, and their masses are given by

$$\begin{aligned}m_{X_R}^2&=m_X^2+\frac12\lambda_{HX}v_H^2+\frac12\lambda_{SX}v_S^2+\sqrt2\mu v_S\\ m_{X_I}^2&=m_X^2+\frac12\lambda_{HX}v_H^2+\frac12\lambda_{SX}v_S^2-\sqrt2\mu v_S.\end{aligned}\tag{8}$$

The S field breaks the $U(1)_{L_\mu-L_\tau}$ symmetry spontaneously by developing a VEV. Since the X field does not develop a VEV, there is a remnant discrete Z_2 symmetry under which the X and Q fields are odd, and the other fields are even. Therefore, the lightest component X_I is stable and becomes a candidate of DM.

The two physical *CP*-even states h and S are from the mixing of h_1 and h_2 by the following relation:

$$\begin{pmatrix}h_1\\h_2\end{pmatrix}=\begin{pmatrix}\cos\theta&\sin\theta\\-\sin\theta&\cos\theta\end{pmatrix}\begin{pmatrix}h\\S\end{pmatrix},\tag{9}$$

where θ is the mixing angle. The two *CP*-even Higgses mediate the DM interactions:

$$\begin{aligned}\mathcal{L}(X_IX_I,h,S)=&-\frac12\left[\lambda_{HX}v_Hc_\theta-(\lambda_{SX}v_S-\sqrt2\mu)s_\theta\right]hX_I^2\\&-\frac12\left[\lambda_{HX}v_Hs_\theta+(\lambda_{SX}v_S-\sqrt2\mu)c_\theta\right]SX_I^2.\end{aligned}\tag{10}$$

In this paper, in order to suppress the stringent constraints from direct and indirect DM detection experiments, we simply assume that the hX_IX_I coupling is absent, namely taking $\theta=0$ and $\lambda_{HX}=0$. For $\theta=0$, we obtain the following expressions:

$$\lambda_{HS} = 0, \quad \lambda_H = \frac{m_h^2}{2v_h^2}, \quad \lambda_S = \frac{m_S^2}{2v_S^2}. \tag{11}$$

After $\mathcal{S}$ obtains a VEV, the $U(1)_{L_\mu - L_\tau}$ gauge boson Z' obtains a mass

$$m_{Z'} = 2g_{Z'}\,|q_x|\,v_S. \tag{12}$$

The complex singlet X mediates the new Yukawa interactions of the vector-like quarks and the SM left-handed quark:

$$\Delta\mathcal{L}_{\text{Yukawa}} = -\frac{1}{\sqrt{2}}\sum_{i=1,2,3}\left(\lambda_{u_i}\bar{u}_{iL}U + \lambda_{d_i}\bar{d}_{Li}D\right)(X_R + iX_I) + \text{h.c.}, \tag{13}$$

where we assume that the down-type quarks are already in the mass basis and rotate the interaction eigenstates of up-type quarks to the mass eigenstates via the CKM matrix V. Thus, $\lambda_{u_i} \equiv \sum_j V_{ij}\lambda_j$ and $\lambda_{d_i} \equiv \lambda_i$ with $u_i = u,c,t$ and $d_i = d,s,b$. We simply set $\lambda_1 = 0$ to remove the constraints related to the first generation quarks. As a result, λ_u is much smaller than λ_c and λ_t due to the suppression of the factors of V_{us} and V_{ub}.

III. $b \to s\mu^+\mu^-$ ANOMALY

In addition to m_h = 125 GeV and v_h = 246 GeV, there are many new parameters in the model, and the input parameters taken in our calculations are shown in Table 2. We can determine other parameters from these input parameters, i.e., v_S from Eq. (12), λ_H from Eq. (11), λ_S from Eq. (11), μ and m_X^2 from Eq. (8), and μ_h^2 and μ_s^2 from Eq. (7).

To maintain the perturbativity of the scalar potential, we conservatively take

$$|\lambda_{SX}| \leqslant 4\pi, \quad |\lambda_X| \leqslant 4\pi. \tag{14}$$

The input mass parameters are scanned over the following ranges:

$$\begin{aligned}
&60\text{ GeV} \leqslant m_{X_I} \leqslant 1\text{ TeV}, \quad 800\text{ GeV} \leqslant m_{X_R} \leqslant 2\text{ TeV},\\
&1\text{ TeV} \leqslant m_Q \leqslant 2\text{ TeV}, \quad 100\text{ GeV} \leqslant m_{Z'} \leqslant 1\text{ TeV},\\
&100\text{ GeV} \leqslant m_S \leqslant 1\text{ TeV}.
\end{aligned} \tag{15}$$

Table 2. Input parameters in our calculations.

$g_{Z'}$	q_x	$m_{Z'}$	$\lambda_{HS}=0$	$\lambda_{HX}=0$	λ_{SX}	λ_X	m_S	m_{X_R}	m_{X_I}	m_Q	λ_b	λ_s

Considering the bound of the neutrino trident process [24], we take $0 < g_{Z'}/m_{Z'} \leqslant$ (550 GeV)$^{-1}$. We choose $0 < q_x \leqslant 3$ and require $g_{Z'}q_x \leqslant 1$ to maintain the perturbativity of the Z' couplings. Imposing $0.1 \leqslant \lambda_{bs}(\equiv \lambda_b\lambda_s) \leqslant 0.3$, we scan over λ_b and λ_s in the ranges

$$0.1 \leqslant \lambda_b \leqslant 1.0, \quad 0.1 \leqslant \lambda_s \leqslant 1.0. \tag{16}$$

The tree-level stability of the potential of Eq. (5) requires

$$\begin{aligned}
&\lambda_H \geqslant 0, \quad \lambda_S \geqslant 0, \quad \lambda_X \geqslant 0, \quad \lambda_{HS} \geqslant -2\sqrt{\lambda_H\lambda_S},\\
&\lambda_{HX} \geqslant -2\sqrt{\lambda_H\lambda_X}, \quad \lambda_{SX} \geqslant -2\sqrt{\lambda_S\lambda_X},\\
&\sqrt{\lambda_{HS}+2\sqrt{\lambda_H\lambda_S}}\sqrt{\lambda_{HX}+2\sqrt{\lambda_H\lambda_X}}\sqrt{\lambda_{SX}+2\sqrt{\lambda_S\lambda_X}}\\
&\quad +2\sqrt{\lambda_H\lambda_S\lambda_X}+\lambda_{HS}\sqrt{\lambda_X}+\lambda_{HX}\sqrt{\lambda_S}+\lambda_{SX}\sqrt{\lambda_H} \geqslant 0.
\end{aligned} \tag{17}$$

We consider four relevant $b \to s$ flavor observables: $R_{K^{(*)}}$, Δm_s, $B \to X_s\gamma$, and $R^{\nu\nu}_{K^{(*)}}$, which are introduced in detail in Ref. [23]. Here, we give the expressions for calculating the four observables briefly.

A. Numerical calculations

1. $R_{K^{(*)}}$ anomalies

The model does not contain the tree-level Z'-b-s flavor-changing coupling but produces the Z'-b-s coupling via a one-loop diagram involving the vector-like quarks X_R and X_I. The $b \to s\mu^+\mu^-$ transition operator O_9^μ is generated by Z'-exchanging penguin diagrams. The corresponding Wilson coefficient $C_9^{\mu,NP}$ is given by [23]

$$C_9^{\mu,\text{NP}} = -\frac{\sqrt{2}q_x}{8G_F m_{Z'}^2}\frac{\alpha_{Z'}}{\alpha_{\text{em}}}\frac{\lambda_s\lambda_b^*}{V_{ts}^*V_{tb}}\left[\frac{1}{2}(k'(x_I)+k'(x_R)) - k(x_I,x_R)\right], \tag{18}$$

where $x_{R,I} = m_{X_{R,I}}^2/m_Q^2$,

$$k(x) = \frac{x^2\log x}{x-1}, \quad k(x_1,x_2) = \frac{k(x_1)-k(x_2)}{x_1-x_2}. \tag{19}$$

The prime on the k functions denotes a derivative with respect to the argument. A large mass splitting between m_{X_R} and m_{X_I} can enhance the absolute value of $C_9^{\mu,\text{NP}}$, which can explain the $R_{K^{(*)}}$ anomaly.

2. Δm_s for $B_s-\bar{B}_s$ mixing, $B \to X_s\gamma$, and $R^{\nu\nu}_{K^{(*)}}$

The model gives new contributions to the $B_s-\bar{B}_s$ mixing via box diagrams involving the vector-like quarks

X_R and X_I, which can be written in the form

$$H_{\rm eff}^{\Delta B=2,{\rm NP}} = C_1^{\rm NP}(\bar{s}\gamma_\mu P_L b)(\bar{s}\gamma^\mu P_L b), \tag{20}$$

where $C_1^{\rm NP}$ is given as [23]

$$C_1^{\rm NP} = \frac{(\lambda_s\lambda_b^*)^2}{128\pi^2 M_D^2}k(1,x_R,x_I), \tag{21}$$

where

$$k(1,x_R,x_I) = \frac{k(1,x_I)-k(x_R,x_I)}{1-x_R}. \tag{22}$$

At the 2σ confidence level, the measurement of the mass difference in the $B_s-\bar{B}_s$ system constrains the value of $C_1^{\rm NP}$ [13] to

$$-2.1\times10^{-11} \leqslant C_1^{\rm NP} \leqslant 0.6\times10^{-11}\,({\rm GeV}^{-2}). \tag{23}$$

The model gives new contributions to $B\to X_s\gamma$ via a one-loop diagram involving the vector-like quarks X_R and X_I. The Wilson coefficients $C_{7\gamma,8g}$ are corrected [23]:

$$C_{7\gamma}^{\rm NP} = \frac{\sqrt{2}}{48}\frac{\lambda_s\lambda_b^*}{V_{ts}^*V_{tb}}\frac{1}{G_F M_D^2}(J_1(x_I)+J_1(x_R)),$$
$$C_{8g}^{\rm NP} = -\frac{\sqrt{2}}{16}\frac{\lambda_s\lambda_b^*}{V_{ts}^*V_{tb}}\frac{1}{G_F M_D^2}(J_1(x_I)+J_1(x_R)), \tag{24}$$

where

$$J_1(x) = \frac{1-6x+3x^2+2x^3-6x^2\log x}{12(1-x)^4}. \tag{25}$$

The experimental measurement of the inclusive branching fraction of $B\to X_s\gamma$ is $(3.32\pm0.15)\times10^{-4}$ [25], and the SM prediction is $(3.36\pm0.23)\times10^{-4}$ [26]. The explanation of experimental values at 2σ level requires

$$-6.3\times10^{-2} \leqslant C_{7\gamma}^{\rm NP}+0.24C_{8g}^{\rm NP} \leqslant 7.3\times10^{-2}. \tag{26}$$

The model gives additional contributions to $B\to K^{(*)}\nu\bar{\nu}$ via diagrams that are obtained by replacing the external muon lines of the $b\to s\mu^+\mu^-$ diagrams with neutrino lines. Current experimental bounds are

$$R_K^{\nu\bar{\nu}}<4.3,\quad R_{K^*}^{\nu\bar{\nu}}<4.4,\quad (\text{at } 90\%\text{C.L.}). \tag{27}$$

with

$$R_{K^{(*)}}^{\nu\bar{\nu}} = \frac{\mathcal{B}(B\to K^{(*)}\nu\bar{\nu})^{\rm exp}}{\mathcal{B}(B\to K^{(*)}\nu\bar{\nu})^{\rm SM}}. \tag{28}$$

In the model, the prediction value of $R_{K^{(*)}}^{\nu\nu}$ is [23]

$$R_{K^{(*)}}^{\nu\bar{\nu}} = \frac{\sum_{i=1}^3\left|C_L^{\rm SM}+C_L^{ii,{\rm NP}}\right|^2}{3\left|C_L^{\rm SM}\right|^2} = 1+\frac{2\left|C_L^{22,{\rm NP}}\right|^2}{3\left|C_L^{\rm SM}\right|^2}, \tag{29}$$

with $C_L^{\rm SM}\approx-6.35$, $C_L^{11,{\rm NP}}=0$, and

$$C_L^{22,{\rm NP}} = -C_L^{33,{\rm NP}} = -\frac{\sqrt{2}q_x}{16G_F m_{Z'}^2}\frac{\alpha_{Z'}}{\alpha_{\rm em}}\frac{\lambda_s\lambda_b^*}{V_{ts}^*V_{tb}}\Big[\frac{1}{2}(k'(x_I)$$
$$+k'(x_R))-k(x_I,x_R)\Big]. \tag{30}$$

B. Results and discussions

After imposing the constraints mentioned above, we use the model to explain the $R_{K^{(*)}}$ anomalies. The bounds of $B\to X_s\gamma$ and $R_{K^{(*)}}^{\nu\nu}$ are almost satisfied in the whole parameter space, being consistent with $R_{K^{(*)}}$. However, there is a strong correlation between Δm_s and $R_{K^{(*)}}$, as shown in Eq. (18) and Eq. (21). Figure 1 shows that $R_{K^{(*)}}$ is explained in the entire regions of 1000 GeV $\leqslant m_Q\leqslant$ 2000 GeV and $0.1\leqslant\lambda_{bs}\leqslant0.3$. However, Δm_s imposes an upper bound on λ_{bs}, which increases with m_Q. Due to the constraints of Δm_s, the $R_{K^{(*)}}$ anomaly can be only explained in the region where $\lambda_{bs}\leqslant0.25$.

After imposing the relevant $b\to s$ flavor observables, neutrino trident process, and theoretical constraints, the

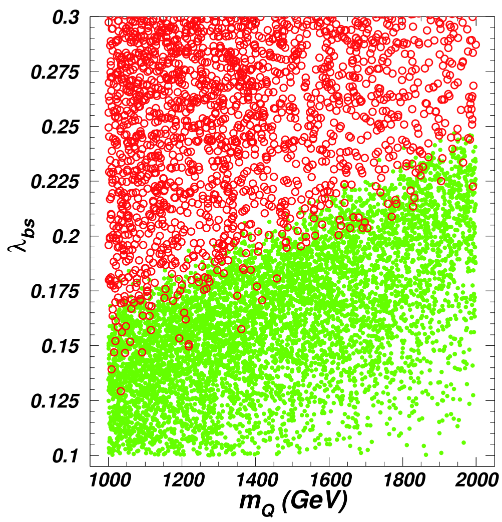

Fig. 1. (color online) Remaining samples projected on the plane of m_Q versus λ_{bs}. All the samples accomodate the $R_{K^{(*)}}$ anomaly, and the bullets (green) and circles (red) are, respectively, the samples allowed and excluded by Δm_s.

samples explaining the $R_{K^{(*)}}$ anomaly are projected on Fig. 2. The left panel shows that the parameters $g_{Z'}q_X$ and $m_{Z'}$ are imposed with strong constraints. Due to the constraints of the neutrino trident process, the region with small $m_{Z'}$ and large $g_{Z'}q_X$ is empty. To accomodate the $R_{K^{(*)}}$ anomaly, $m_{Z'}$ must increase with $g_{Z'}q_X$. Since we take $g_{Z'}q_x \leqslant 1$ to maintain the perturbativity of the Z' couplings, $m_{Z'} >$ 600 GeV is excluded. Similarly, $g_{Z'}q_X \leqslant 0.2$ is disfavored since the minimal value of $m_{Z'}$ is taken as 100 GeV.

The right panel of Fig. 2 shows that m_{X_I} must increase with m_{X_R} since a sizable mass splitting between m_{X_R} and m_{X_I} is favoured to explain the $R_{K^{(*)}}$ anomaly. Because we choose $m_{X_R} \leqslant 2$ TeV, m_{X_I} must be smaller than 900 GeV. Similarly, $m_{X_R} \leqslant 800$ GeV is disfavored since the minimal value of m_{X_I} is taken as 60 GeV.

IV. DARK MATTER

In the chosen parameter space, the DM can be annihilated into $Z'Z'$, SS, and the SM quarks. The corresponding Feynman diagrams are shown in Fig. 3. The $X_I X_I \to q\bar{q}$ processes proceed through the $D(U)$-exchanging t-channel diagrams. For 1 TeV $\leqslant m_Q \leqslant$ 2 TeV, $\lambda_b < 1$, and $\lambda_s < 1$, the annihilation cross sections are very small, and their contributions to the relic density can be ignored. The $X_I X_I \to SS$ processes proceed through the S-exchanging s-channel diagram and the diagram of the quartic coupling $X_I X_I SS$. The $X_I X_I \to Z'Z'$ processes proceed through the S-exchanging s-channel diagram, X_R-exchanging t-channel diagram, and diagram of the quartic coupling $X_I X_I Z'Z'$.

We use micrOMEGAs [27] to calculate the relic density and the spin-independent DM-nucleon cross section. The model file is generated by FeynRules [28]. The Planck collaboration reported the relic density of cold DM in the universe as $\Omega_c h^2 = 0.1198 \pm 0.0015$ [29].

The annihilation cross section of $X_I X_I \to Z'Z'$ from the diagram shown in Fig. 3(c) only depends on the parameters $g_{Z'}q_X$, $m_{Z'}$, and m_{X_I}. Since the $R_{K^{(*)}}$ anomaly imposes a lower bound on $g_{Z'}q_X$, our calculations show that the annihilation cross sections of $X_I X_I \to Z'Z'$ are much larger than the value that produces the correct relic density for $m_{Z'} < m_{X_I}$. Similarly, we find that the annihilation cross sections of $X_I X_I \to SS$ are too large to obtain the correct relic density for $m_S < m_{X_I}$. The main reason is that the $R_{K^{(*)}}$ anomaly imposes a low bound on the $SX_I X_I$ coupling. The $R_{K^{(*)}}$ anomaly requires a large mass splitting between X_R and X_I and imposes a lower bound on the parameter μ according to Eq. (8):

$$\sqrt{2}\mu = \frac{m_{X_R}^2 - m_{X_I}^2}{2v_S}. \tag{31}$$

From Eq. (10), we can obtain the coupling of $SX_I X_I$ for the chosen parameters:

$$\lambda_{SX_I X_I} = \sqrt{2}\mu - \lambda_{SX} v_S. \tag{32}$$

The remaing samples that explain the $R_{K^{(*)}}$ anomaly in Fig. 2 are projected on the planes of $\lambda_{SX_I X_I}$ versus λ_{SX} and $m_S - m_{X_I}$ in Fig. 4. From Fig. 4, we find that the $R_{K^{(*)}}$ anomaly requires $\sqrt{2}\mu > 3500$ GeV, which dominates the value of $\lambda_{SX_I X_I}$. $\lambda_{SX_I X_I}$ tends to decrease with increasing λ_{SX} and v_S, and $\lambda_{SX_I X_I}$ is reduced to around 1000 GeV for $\lambda_{SX} \approx 4\pi$ and $v_S \approx 400$ GeV. Meanwhile, a large v_S can increase m_S, leading to $m_S > m_{X_I}$. The right-most panel in Fig. 4 shows that the minimal value of $\lambda_{SX_I X_I}$ is approximately 4000 GeV for $m_S < m_{X_I}$.

To produce the relic density via the $X_I X_I \to Z'Z', SS$ annihilation processes, we need to use the effects of for-

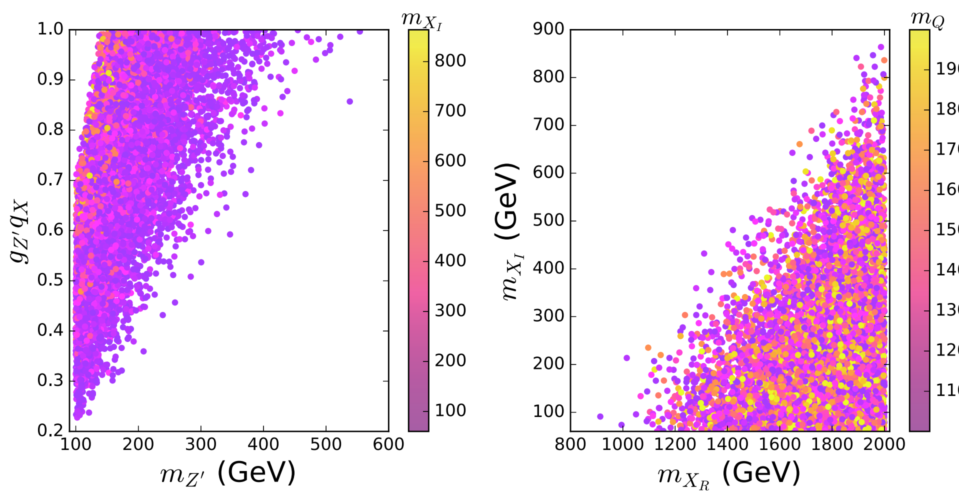

Fig. 2. (color online) All the samples accomodate the $R_{K^{(*)}}$ anomaly and satisfy the relevant $b \to s$ flavor observables, neutrino trident process, and theoretical constraints.

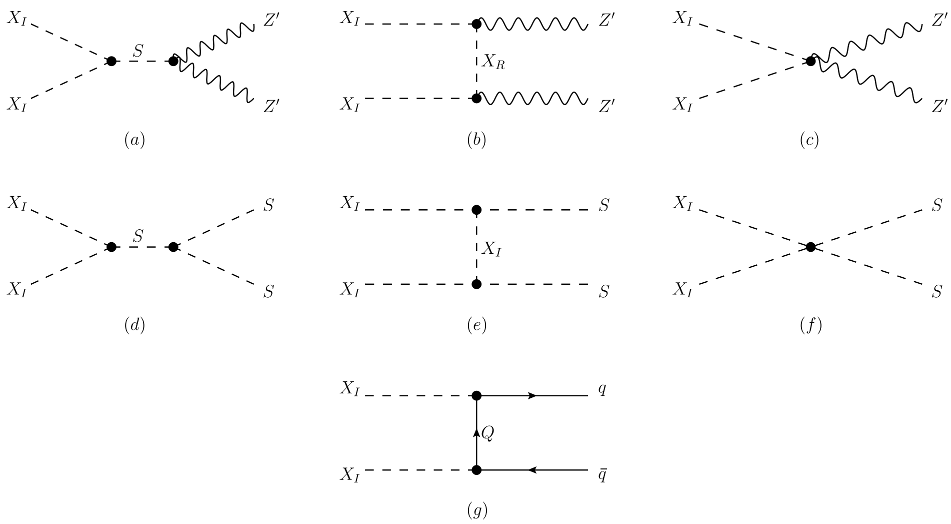

Fig. 3. Feynman diagrams of $X_I X_I \to Z'Z'$, SS, $q\bar{q}$processes.

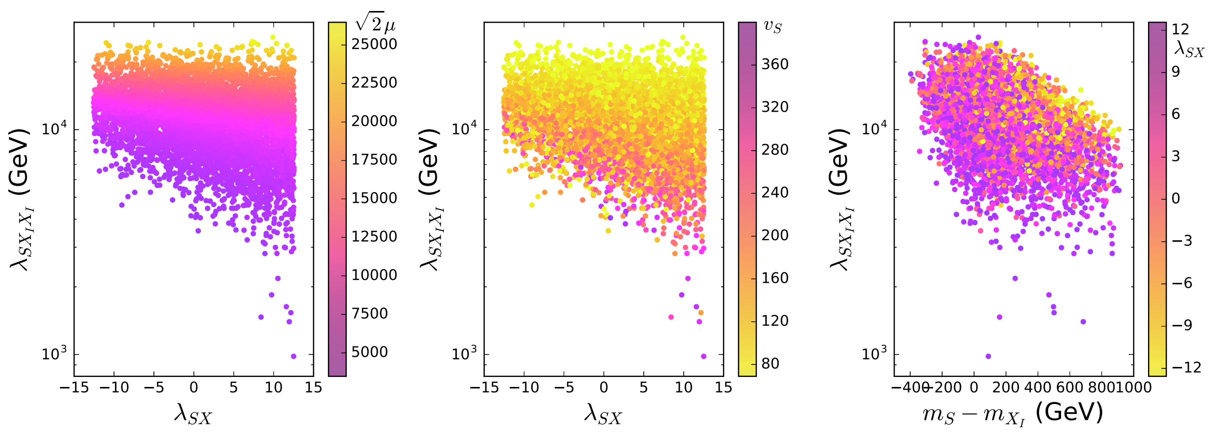

Fig. 4. (color online) Same as Fig. 2 but projected on the planes of $\lambda_{SX_IX_I}$ versus λ_{SX} and $m_S - m_{X_I}$.

bidden channel, namely that $m_{Z'}$ or m_S is appropriately larger than m_{X_I}. In the calculation of the thermal averaged cross section, the early universe kinetic energy of the DM is nonnegligible. When the mass difference is not too large and the DMs move fast, the center of mass energy exceeds twice $m_{Z'}$ or m_S. Therefore, the process $X_I X_I \to Z'Z'$ (SS) can occur in the early universe when m_{X_I} is appropriately different from $m_{Z'}$ (m_S). In addition, the temperature at the present time is much lower than the freeze-out temperature, and the velocity of DM is much smaller than that in the early universe. The channels $X_I X_I \to Z'Z'$ (SS) are kinematically forbidden at the present time; therefore, the experimental constraints of the indirect detection of DM can be naturally satisfied.

After imposing the constraints of "pre-DM" (denoting the $R_{K^{(*)}}$ anomaly, relevant $b \to s$ flavor observables, neutrino trident process, and theoretical constraints), we find some samples that can produce the correct DM relic density. The remaining samples are projected in Fig. 5. From the left panel, we find that the relic density favors $m_{X_I} <$ 350 GeV and most of the surviving samples lie in the region where $m_{Z'} - m_{X_I} <$ 60 GeV. For a large m_S, the annihilation cross section of $X_I X_I \to Z'Z'$ from the diagram in Fig. 3(a) is suppressed. Therefore, a small value of $m_{Z'} - m_{X_I}$ is required to enhance the cross section. For a large value of $m_{Z'} - m_{X_I}$, the $X_I X_I \to Z'Z'$ channel is still forbidden in the early universe and does not contribute to the relic density. For such a case, the $X_I X_I \to SS$ channel will have the dominant contribution to the relic density. As shown in the right panel, for a large value of $m_{Z'} - m_{X_I}$, a small value of $m_S - m_{X_I}$ is required to allow the $X_I X_I \to SS$ channel in the early universe.

Exchanging an initial state X_I and a final state quark shown in Fig. 3(f), we can obtain the Feynman diagrams that contribute to the cross section of the DM scattering off the nuclei. In the chosen parameter space, we find that the bounds of the XENON1T fail to exclude the parameter space that achieves the correct relic density [30].

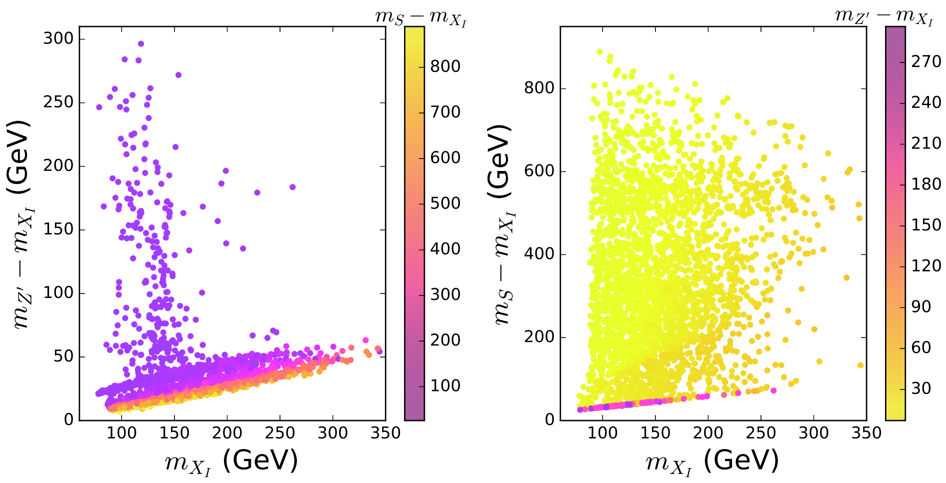

Fig. 5. (color online) Remaining samples satisfying the DM relic density and the constraints of "pre-DM."

V. THE DARK MATTER, Z', AND VECTOR-LIKE QUARK AT THE LHC

A. Current constraints from direct searches at the LHC

At the LHC, the vector-like quarks D and U are produced in pairs via the QCD processes

$$pp \to D\bar{D}, U\bar{U}. \tag{33}$$

In the chosen parameter space, D and U have the following decay modes:

$$D \to X_I d_i, X_R d_i, \quad U \to X_I u_i, X_R u_i \tag{34}$$

with

$$X_R \to X_I Z' \to X_I \mu^+\mu^-,\ X_I \tau^+\tau^-,\ X_I \nu_\mu \bar{\nu}_\mu,\ X_I \nu_\tau \bar{\nu}_\tau. \tag{35}$$

Since the $R_{K^{(*)}}$ anomaly and the DM relic density favor X_R to be much larger than X_I, D and U will mainly decay into $X_I s$, $X_I b$, and $X_I u_i$. In this paper, the coupling of X_I and the d quark is taken as zero.

In order to restrict the products of the above processes at the LHC for our model, we perform simulations for the samples using `MG5_aMC-2.7.3` [31] with `PYTHIA8` [32] and `Delphes-3.2.0` [33], and adopt the constraints from all the 13 TeV LHC analysis in the version `CheckMATE 2.0.28` [34]. For the excluded samples, the most sensitive experimental analysis is the ATLAS search for squarks and gluinos in final states that contain jets and missing transverse momentum at the 13 TeV LHC with 139 fb^{-1} integrated luminosity data [35]. The final states $E_T^{\rm miss}$ + jets are just the main signals of $D\bar{D}$ and $U\bar{U}$ in the model.

In Fig. 6, all the samples satisfy the constraints of the "pre-DM" and DM observables. Current direct searches at the LHC exclude $m_Q <$ 1.7 TeV. For a large λ_s, some samples with m_Q around 1.8 TeV can also be excluded. With an increase of m_Q, the production cross sections of $pp \to D\bar{D}$, $U\bar{U}$ are suppressed by the phase space, and the direct searches at the LHC can be satisfied.

B. The searches for the new particles at the high luminosity LHC

Since the vector-like quarks U and D are charged under $U(1)_{L_\mu - L_\tau}$, the gauge boson Z' has tree-level couplings to the vector-like quarks. Therefore, the model provides a novel approach of searching for Z', the vector-like quark, and DM. Z' is produced via the QCD process followed by $D \to s(b)X_I$, $D \to s(b)X_R \to s(b)Z'X_I$, and then $Z' \to \mu^+\mu^-$.

We pick a benchmark point which accomodates the $b \to s\mu^+\mu^-$ anomaly and satisfies the constraints of "pre-DM," the DM observables, and the current searches at the LHC. Several key input and output parameters are shown in Table 3. Now we perform detailed simulations on the signal and backgrounds at the 14 TeV LHC with high luminosity. We choose the signal to contain an opposite sign di-muon ($\mu^+\mu^-$), missing transverse momentum $E_T^{\rm miss}$, and multijets ($\geqslant$ 2 jets), which include at least one b-jet. The major SM irreducible background processes to this signal are $t\bar{t}$, WW+ jets, ZZ+ jets, and WZ+ jets.

We identify muon candidates by requiring them to have $p_T >$ 15 GeV and $|\eta| < 2.5$. The anti-kt algorithm is employed to reconstruct jets with a radius parameter $R = 0.4$ [36], and the jets are required to have $p_T >$ 20 GeV and $|\eta| < 2.5$. We assume an average b-tagging efficiency of 80% for real b-jets.

In order to suppress the contributions from the SM process, we apply the "stransverse" mass m_{T2} [37-39] defined as

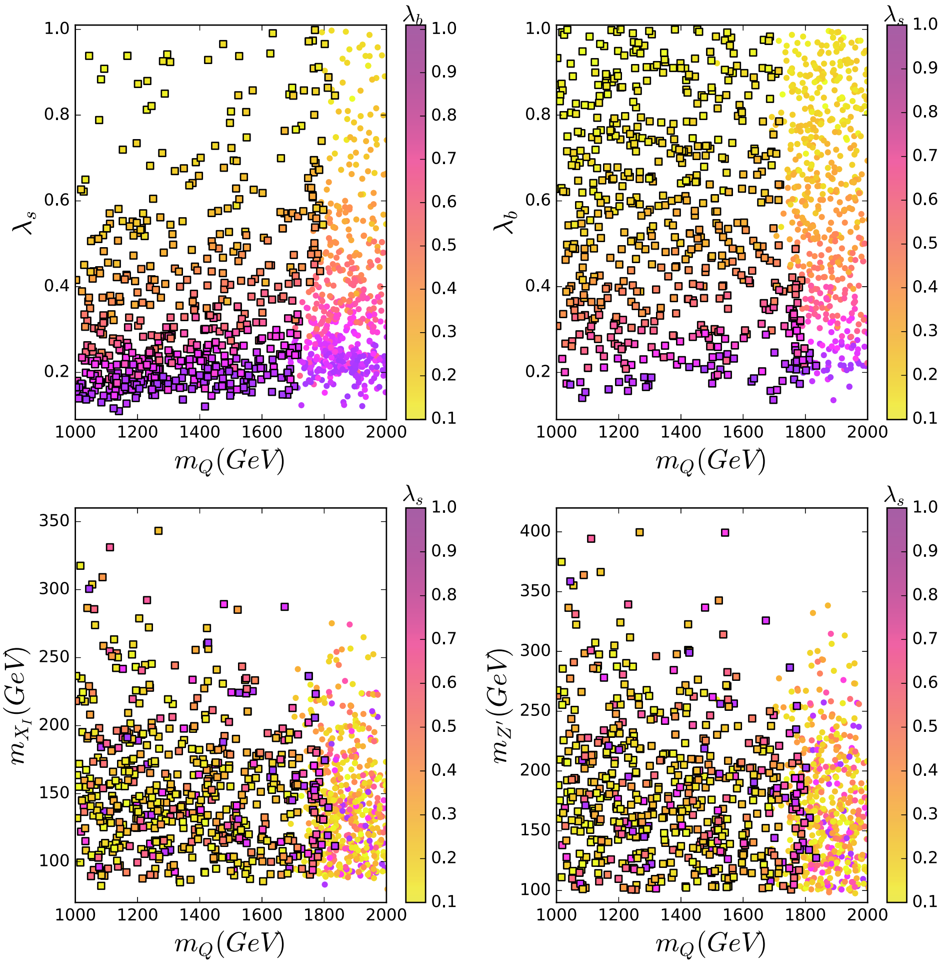

Fig. 6. (color online) All the samples satisfy the constraints of the "pre-DM" and DM observables. The squares and bullets indicate, respectively, the samples excluded and allowed by the current direct searches at the LHC.

Table 3. Several key input and output parameters for the benchmark point.

$m_{Z'}$/GeV	m_{X_I}/GeV	m_{X_R}/GeV	m_Q/GeV	Br$(D\to X_I b)$	Br$(D\to X_I s)$	Br$(D\to X_R b)$	Br$(D\to X_R s)$
170	145	1309	1930	0.63	0.14	0.19	0.04

$$m_{T2}=\min_{q_T}\left[\max\left(m_T(\boldsymbol{p}_T^{\ell_1},\boldsymbol{q}_T),m_T(\boldsymbol{p}_T^{\ell_2},\boldsymbol{p}_T^{\rm miss}-\boldsymbol{q}_T)\right)\right],\quad(36)$$

where $\boldsymbol{p}_T^{\ell_1}$ and $\boldsymbol{p}_T^{\ell_2}$ are the transverse momenta of the di-muon. $\boldsymbol{q}_T$ is a transverse vector that minimizes the larger of the two transverse masses m_T:

$$m_T(\boldsymbol{p}_T,\boldsymbol{q}_T)=\sqrt{2(p_Tq_T-\boldsymbol{p}_T\cdot\boldsymbol{q}_T)}.\qquad(37)$$

Figure 7 shows the distributions of some kinematical variables at the LHC with $\sqrt{s}=14$ TeV for the signal and the background $t\bar{t}$. The other processes are not shown since they are subdominant. According to the distribution differences between the signal and backgrounds, we can improve the ratio of signal to background by making some kinematical cuts. We impose the following cuts:

$$P_T^{j_1}>290\ {\rm GeV},\ P_T^{j_2}>60\ {\rm GeV},\ P_T^{b_1}>60\ {\rm GeV},$$
$$\Delta R_{\mu^+\mu^-}<2.0,\ 150\ {\rm GeV}<M_{\mu^+\mu^-}<180\ {\rm GeV},$$
$$E_T^{\rm miss}>310\ {\rm GeV},\ m_{T2}>100\ {\rm GeV},\ H_T^{b\ell}>500\ {\rm GeV}.\quad(38)$$

Here, $P_T^{j_1}$ and $P_T^{j_2}$ denote the transverse momentum of the hardest and the second hardest jets, which include the b-jet, and $P_T^{b_1}$ denotes the transverse momentum of the hardest b-jet. $\Delta R=\sqrt{(\Delta\phi)^2+(\Delta\eta)^2}$ is the particle separation with $\Delta\phi$ and $\Delta\eta$ being the separation in the azimuthal angle and rapidity, respectively. $M_{\mu^+\mu^-}$ is the invariant mass of μ^+ and μ^-, and $H_T^{b\ell}$ is a scalar sum of the transverse momenta of all the b-jets, $\mu^\pm$. Since μ^+ and μ^- of

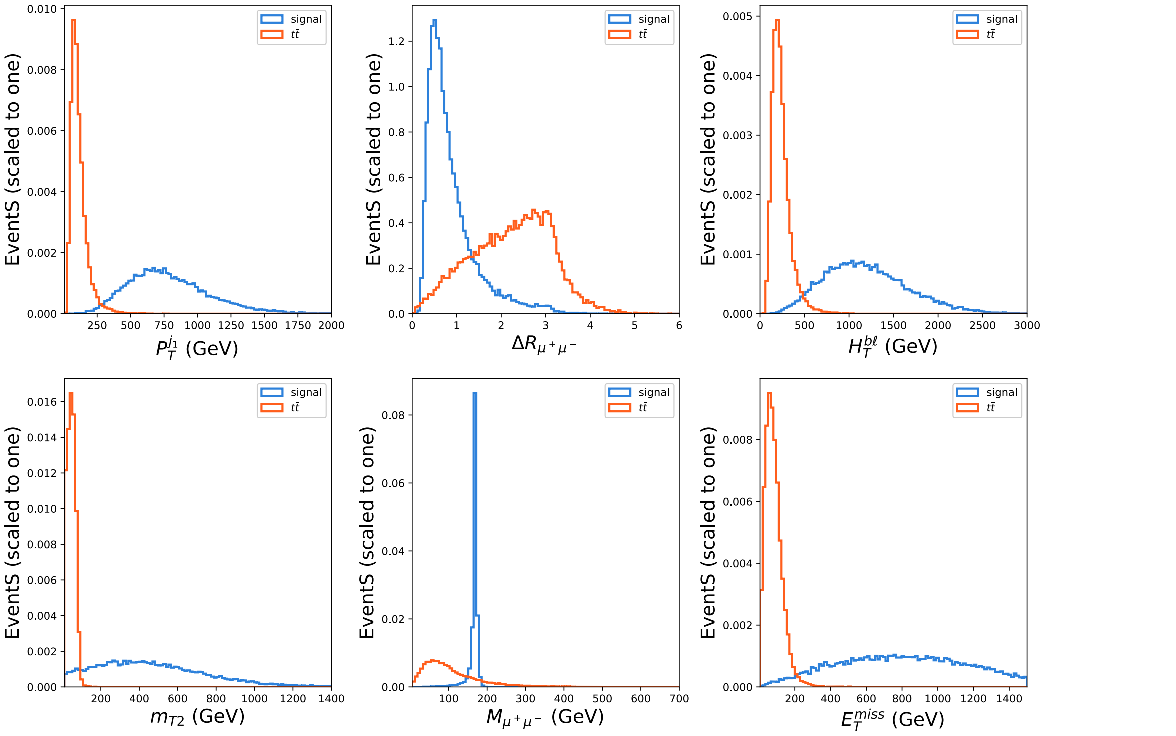

Fig. 7. (color online) Signal and $t\bar{t}$ background distributions of $P_T^{j_1}$, $\Delta R_{\mu^+\mu^-}$, $H_T^{b\ell}$, m_{T2}, $M_{\mu^+\mu^-}$, and $E_T^{\rm miss}$ at the 14 TeV LHC after requiring an opposite sign di-muon and multijets ($\geq$ 2 jets), which include at least one b-jet.

the signal are from the decay of Z' with a mass of 170 GeV, a $M_{\mu^+\mu^-}$ peak appears at 170 GeV, and $\Delta R_{\mu^+\mu^-}$ favors a small value. The jets, X_I, and $\mu^\pm$ of the signal are the decay products of the vector-like quark with a mass of 1930 GeV, and such a heavy mass results in these products tending to have large transverse momenta. The distributions of m_{T2} for $t\bar{t}$ and WW+jets backgrounds peak before m_W. In addition, the DM X_I has a mass of 145 GeV, therefore the signal events tend to have a large $E_T^{\rm miss}$.

We compute the significance as $\mathbf{S} = \dfrac{n_s}{\sqrt{n_s+n_b}}$, where n_s and n_b are the normalized signal and background event yields, respectively. After making the kinematical cuts of Eq. (38), n_b is drastically reduced and dominated by n_s. For example, $n_s \sim 33$ and $n_s + n_b \sim 35$ for a dataset wtih 3000 fb^{-1} at the 14 TeV LHC. Figure 8 shows that, for the benchmark point, the significance can reach 2σ and 5.6σ at the 14 TeV LHC with integrated luminosities 400 fb^{-1} and 3000 fb^{-1}.

The gauge boson Z' is also produced via $pp \to D\bar{D}$ followed by both D decays to X_R, i.e. $D \to s(b)X_R \to s(b)Z'X_I$ and $\bar{D} \to \bar{s}(\bar{b})X_R \to \bar{s}(\bar{b})Z'X_I$. Because of two Z' in this channel, the final signal contains two di-muons, missing transverse momentum $E_T^{\rm miss}$, and multijets ($\geqslant$ 2 jets). Since the $R_{K^{(*)}}$ anomaly requires m_{X_R} to be much larger than m_{X_I}, Br$[D \to s(b)X_R]$ is much smaller than Br$[D \to s(b)X_I]$. In addition, the second Z' decay into

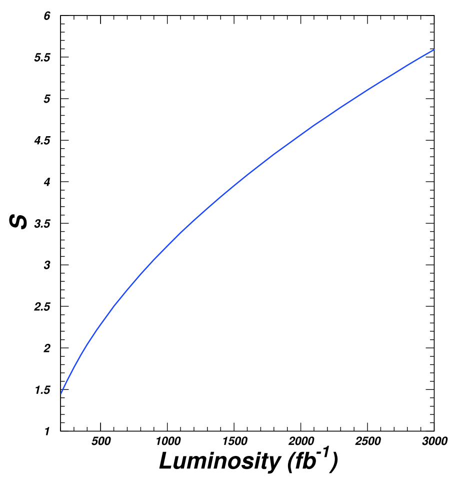

Fig. 8. (color online) Significance versus integrated luminosity of the 14 TeV LHC for the benchmark point.

$\mu^+\mu^-$ will lead to an additional suppression factor of $\dfrac{1}{3}$. Taking the benchmark point in Table 3 as an example, we can obtain

$$\frac{{\rm Br}(D\bar{D} \to b\bar{b}X_IX_R \to b\bar{b}X_IX_IZ' \to b\bar{b}X_IX_I\mu^+\mu^-)}{{\rm Br}(D\bar{D} \to b\bar{b}X_RX_R \to b\bar{b}X_IX_IZ'Z' \to b\bar{b}X_IX_I\mu^+\mu^-\mu^+\mu^-)} \approx 20. \tag{39}$$

Although the two di-muons of the $D\bar{D} \to X_RX_Rb\bar{b}$

channel can be used to suppress the background events more efficiently, the number of signal events is approximately one twentieth of that of the $D\bar{D} \to X_I X_R b\bar{b}$ channel. Therefore, the channel studied in detail in this paper is more promising for probing Z' than the channel of both D decays to X_R.

VI. CONCLUSION

In this study, we investigate the capability of the LHC to test DM, Z', and vector-like quarks in a local $U(1)_{L_\mu - L_\tau}$ model in light of the $b \to s\mu^+\mu^-$ anomaly and DM observables. We take $m_Q < 2$ TeV and $m_{X_R} < 2$ TeV and find that the $b \to s\mu^+\mu^-$ anomaly and the DM observables favor $m_{X_I} < 350$ GeV and $m_{Z'} < 450$ GeV after imposing relevant constraints from theory and $b \to s$ flavor observables. The current searches for jets and missing transverse momentum at the 13 TeV LHC with 139 fb^{-1} integrated luminosity data exclude $m_Q < 1.7$ TeV. Finally, we propose a novel channel for probing these new particles at the high luminosity LHC via the QCD process $pp \to D\bar{D}$ followed by $D \to s(b)X_I$, $D \to s(b)Z'X_I$, and then $Z' \to \mu^+\mu^-$. Taking a benchmark point of $m_Q = 1.93$ TeV, $m_{Z'} = 170$ GeV, and $m_{X_I} = 145$ GeV, we perform a detailed Monte Carlo simulation and find that this benchmark point can be accessed at the 14 TeV LHC with an integrated luminosity 3000 fb^{-1}.

ACKNOWLEDGMENT

We thank Biaofeng Hou for the helpful discussions.

References

[1] R. Aaij *et al.* (LHCb Collaboration), Phys. Rev. Lett. **113**, 151601 (2014)
[2] R. Aaij *et al.* (LHCb Collaboration), Phys. Rev. Lett. **122**, 191801 (2019)
[3] R. Aaij *et al.* (LHCb Collaboration), JHEP **1708**, 055 (2017)
[4] M. Prim (for the Belle Collaboration), arXiv: 1904.02440
[5] A. Datta, J. Kumar, and D. London, Phys. Lett. B **797**, 134858 (2019)
[6] X. G. He, G. C. Joshi, H. Lew *et al.*, Phys. Rev. D **43**, 2224 (1991)
[7] A. Crivellin, G. DAmbrosio, and J. Heeck, Phys. Rev. Lett. **114**, 151801 (2015)
[8] W. Altmannshofer, S. Gori, S. Profumo *et al.*, JHEP **12**, 106 (2016)
[9] C.-H. Chen and T. Nomura, Phys. Lett. B **777**, 420427 (2018)
[10] S. Baek, Phys. Lett. B **781**, 376382 (2018)
[11] W. Altmannshofer, S. Gori, M. Pospelov *et al.*, Phys. Rev. D **89**, 095033 (2014)
[12] W. Altmannshofer and I. Yavin, Phys. Rev. D **92**, 075022 (2015)
[13] P. Arnan, L. Hofer, F. Mescia *et al.*, JHEP **04**, 043 (2017)
[14] S. Singirala, S. Sahoo, and R. Mohanta, Phys. Rev. D **99**, 035042 (2019)
[15] P. T. P. Hutauruk, T. Nomura, H. Okada *et al.*, Phys. Rev. D **99**, 055041 (2019)
[16] A. Biswas and A. Shaw, JHEP **05**, 165 (2019)
[17] Z.-L. Han, R. Ding, S.-J. Lin *et al.*, Eur. Phys. Jour. C **79**, 1007 (2019)
[18] A. S. Joshipura, N. Mahajan, and K. M. Patel, JHEP **03**, 001 (2020)
[19] L. Bian, H. M. Lee, and C. B. Park, Eur. Phys. Jour. C **78**, 306, arXiv:2008.03629
[20] G. H. Duan, X. Fan, M. Frank *et al.*, Phys. Lett. B **789**, 54-58 (2019)
[21] P. Ko, T. Nomura, and H. Okada, Phys. Rev. D **95**, 111701 (2017)
[22] D. Liu, J. Liu, C. E. M. Wagner *et al.*, JHEP **06**, 150 (2018)
[23] S. Baek, JHEP **05**, 104 (2019)
[24] W. Altmannshofer, S. Gori, M. Pospelov *et al.*, Phys. Rev. Lett. **113**, 091801 (2014)
[25] Y. Amhis *et al.*, arXiv: 1612.07233
[26] M. Misiak *et al.*, Phys. Rev. Lett. **114**, 221801 (2015)
[27] G. Belanger, F. Boudjema, A. Pukhov *et al.*, Comput. Phys. Commun. **185**, 960-985 (2014)
[28] A. Alloul *et al.*, Comput. Phys. Commun. **185**, 2250 (2014)
[29] Planck Collaboration, Astron. Astrophys. A **27**, 594 (2016)
[30] E. Aprile *et al.* (XENON Collaboration), arXiv: 1805.12562
[31] J. Alwall *et al.*, JHEP **1407**, 079 (2014)
[32] P. Torrielli and S. Frixione, JHEP **1004**, 110 (2010)
[33] J. de Favereau *et al.* (DELPHES 3 Collaboration), JHEP **1402**, 057 (2014)
[34] D. Dercks, N. Desai, J. S. Kim *et al.*, Comput. Phys. Commun. **221**, 383 (2017)
[35] ATLAS Collaboration, ATLAS-CONF-2019-040
[36] M. Cacciari, G. P. Salam, and G. Soyez, JHEP **0804**, 063 (2008)
[37] C. Lester and D. Summers, Phys. Lett. B **463**, 99 (1999)
[38] A. Barr, C. Lester, and P. Stephens, J. Phys. G **29**, 2343 (2003)
[39] H.-C. Cheng and Z. Han, JHEP **12**, 063 (2008)